

UNCLASSIFIED

Defense Technical Information Center
Compilation Part Notice

ADP023845

TITLE: Unsteady Gas Laser Simulation

DISTRIBUTION: Approved for public release, distribution unlimited

This paper is part of the following report:

TITLE: Proceedings of the HPCMP Users Group Conference 2004. DoD High Performance Computing Modernization Program [HPCMP] held in Williamsburg, Virginia on 7-11 June 2004

To order the complete compilation report, use: ADA492363

The component part is provided here to allow users access to individually authored sections of proceedings, annals, symposia, etc. However, the component should be considered within the context of the overall compilation report and not as a stand-alone technical report.

The following component part numbers comprise the compilation report:
ADP023820 thru ADP023869

UNCLASSIFIED

Unsteady Gas Laser Simulation

Timothy J. Madden

*Air Force Research Laboratory, Directed
Energy Directorate (AFRL/DE), Kirtland AFB,
NM*

timothy.madden@kirtland.af.mil

James H. Miller

*Air Force Research Laboratory, Air Vehicles
Directorate (AFRL/VA), Wright-Patterson AFB,
OH*

james.miller4@wpafb.af.mil

1. Introduction

Theoretical models for chemical lasers depend on a variety of assumptions and empirical data to provide closure and simplify solution of the governing equations. Among the various assumptions and empirical data that have been built into models for chemical lasers are assumptions regarding flow steadiness in the time domain and geometric similarity of the spatial domain. The work discussed here is directed toward elucidating and increasing the understanding of these assumptions commonly used in chemical laser simulation and the impact of their usage upon the predictions of these models. These efforts in turn are directly linked to efforts to achieve improved chemical laser efficiencies and performance, as excursions outside the assumed to be 'well understood' traditional operational parameter space are increasingly necessary.

2. Problem and Methodology

Previous work by Madden and Miller^[1] presented computational data of the chemical oxygen-iodine laser (COIL) indicating that the flowfield should be marked by substantial flow unsteadiness. Although COIL experiment data does not exist to confirm this prediction, non-reacting flow experiments at similar flow conditions do substantiate this prediction. Building on the earlier results, the objective of this work is to further elucidate the flow unsteadiness, its underlying physics, and the manifested effects in COIL performance.

The gas flows within chemical lasers can best be described as the flow of particles of different chemical composition with collisional interactions occurring between the particles and between the particles and the photons within the radiation field. Mathematically, this flow of particles is treated as a continuum and is approximated by the Navier-Stokes continuity equations

for mass, momentum, and energy. In integral form, these equations are given by:

$$\frac{\partial}{\partial t} \iiint_{vol} \langle Q \rangle dvol + \oint_A (\vec{F} - \vec{F}_v) \cdot \hat{n} dA = \iiint_{vol} \langle S \rangle dvol$$

where $\langle Q \rangle$ is the vector of the cell averaged conserved quantities of species density, momentum component, and pressure; \vec{F} and \vec{F}_v are the inviscid and viscous fluxes of the conserved quantities at the cell boundary, and $\langle S \rangle$ is the vector of cell averaged sources of the conserved quantities.

The computational fluid dynamics (CFD) codes GASP and COBALT₆₀ are employed to solve these equations for the simulations performed here. Both codes employ domain decomposition for distribution of the computation among multiple processors on parallel architectures, with inner-iteration methods used to maintain fully implicit, time accurate integration of the solutions.

Reacting flow, i.e., COIL, and non-reacting flow simulations are performed in this work. COIL flowfield simulations are performed using GASP, and non-reacting flow simulations are performed using both GASP and COBALT₆₀. The GASP COIL model utilizes 10 species of mass conservation equations for the chemically reacting components of the COIL flow in addition to the base conservation equations for momentum and energy. An effective binary diffusion model is used to describe concentration and pressure contributions to mass diffusion, an important process in the low density COIL flowfield. A 10 species, 22 reaction finite-rate chemistry mechanism^[2] is used to model the gas phase chemical kinetic processes that generate the population inversion in atomic iodine necessary for laser oscillation in COIL. The computational grid used for this simulation consists of 3 blocks and 3 million grid cells. The computational domain which this grid discretizes represents the smallest geometrically similar element within the COIL experiment flowfield hardware, denoted a 'unit-cell.' The

unit-cell consists of a supersonic ($M \sim 2.2$) converging-diverging nozzle section with one-half of a large and one small injector orifice that issue reactants into the primary flow through this nozzle. Figure 1 illustrates the unit-cell within the context of a mechanical drawing of the experiment's mixing nozzle. The orifices inject a sonic mixture of He and I_2 into a subsonic primary flow composed of He, $O_2(^1\Delta)$, $O_2(^3\Sigma)$, H_2O , and Cl_2 with the complex 3-D flow structure associated with the jet issuing from the orifice providing the mechanism that mixes the two flows. Boundary conditions accomplish the unit-cell approximation through the enforcement of planar symmetry at the nozzle centerline in the vertical direction and at the side boundaries in the lateral direction. No-slip constant temperature boundary conditions are used at the wetted surfaces of the nozzle and orifices, with the temperature fixed at 400 K at the orifice walls and 300 K at the nozzle walls. The nozzle subsonic inflow boundary condition fixes the total pressure and total temperature and the species fractions at constant values, while the derivative of the pressure is set to 0. The nozzle outflow boundary condition sets the second derivative of dependent variables to 0 as is appropriate for supersonic flows.

The non-reacting flow simulations using COBALT₆₀ and GASP are used to diagnose and understand the unsteady COIL simulations. The first non-reacting flow simulation is for the jet-in-crossflow experiment of Fric and Roshko^[3]. This experiment, while performed for subsonic flow injection into a subsonic flow, is similar in terms of the crossflow Reynolds number and the ratio of secondary to primary flows to the COIL flow. Additionally, extensive data documenting the unsteady characteristics of this flow was generated, providing points for comparison of the models used in this work with experiment data on a one-to-one basis. In this simulation, COBALT₆₀ models secondary He injection into a He primary; He is the dominant component of COIL flows whereas the flow parameters of Reynolds number and secondary-to-primary flow ratio for this simulation match the Fric and Roshko^[3] experiment. Subsonic inflow boundary conditions are used for the primary and secondary inflow conditions, with Riemann invariant far-field conditions used at the outflow boundaries. Solid surfaces are treated as no-slip boundaries. An important point to note with regard to this simulation is the fact that the model for the experiment hardware used in this simulation does not split the injector orifice as has been done previously in COIL simulation. This will facilitate assessment of the method in which COIL simulations have been constructed. The computational grid for this simulation is shown in Figure 2.

The second non-reacting flow simulation follows naturally from the COIL simulation and the simulation of

the Fric and Roshko experiment discussed above. This model simulates the COIL hardware but using the method in the Fric and Roshko experiment simulation where the injector orifice is not split with a symmetry plane boundary but is modeled in full. This creates traceability from the Fric and Roshko simulation to simulations of COIL hardware, facilitating understanding of the mechanisms underlying unsteadiness in these flows. The computational grid used in this simulation differs from the first COIL grid in several other ways. First, the streamwise extent of the computational domain ends with the end of the isentropic expansion region of the supersonic nozzle, focusing computational effort on the injection region and transonic region of the throat. The second difference is the grid structure, with the new grid utilizing a multi-block, highly orthogonal topology that substantially increases the grid quality. Finally, this grid contains 64 million grid cells as compared to the 3 million grid cells used in the domain for the previous simulation. The boundary conditions for this simulation remain the same as those used in the COIL simulation, with the exception of the lateral boundaries. In the COIL simulation, the lateral boundaries are modeled as symmetry planes whereas in this simulation they are treated as periodic boundaries where waves exiting from one boundary enter through the opposite and vice versa. This facilitates capturing lateral fluctuations in the flow. The physical model itself differs in that the primary and secondary flows both consist entirely of He. This approximation will drastically reduce computational cost, while still allowing examination of the underlying mechanisms of the flow unsteadiness. GASP is used for execution of this model. Figure 3 illustrates this grid.

COBALT₆₀ and GASP references providing additional details beyond the scope of this paper may be found with Strang, et al.^[4], Miller, et al.^[5], and Madden, et al.^[6,7].

3. Results

We begin by reviewing and updating previous results from unsteady simulation of COIL. The 3-D GASP model for the COIL flowfield was executed in time accurate mode utilizing 1st order accurate time integration with 3rd order spatial accuracy at a physical timestep of 1.0×10^{-8} sec. The computation was advanced to a physical time of 0.001 sec, corresponding to 100,000 time steps in the computation. The physical time of 0.001 sec provides sufficient advancement of the computation to address the characteristics of the predicted flow unsteadiness.

The time accurate execution of the GASP COIL model generated a prediction of the presence of flow unsteadiness that did not decay over the 0.001 sec interval

that the computation was advanced. The unsteadiness was found to extend from the jet/primary interaction region at the point of the He/I₂ transverse injection and continuing downstream undiminished. Figure 4 illustrates the resulting impact of the flow unsteadiness upon the structure of the flow within the He/I₂ jet. Here an isosurface of 0.001 constant I₂ mole fraction, a value of approximately 1% of the concentration in the pure He/I₂, is plotted within 3-D space. The surface demonstrates the presence of a regular, periodic structures associated with unsteady vortex generation, with the structures present in the flow from both the large and small orifices. Since molecular diffusion, i.e., mixing, and chemical reaction are strongly correlated with spatial gradients of reactant concentration, the presence of these unsteady flow structures is expected to have a considerable impact upon this model's predictions of device performance. The evidence of this impact is shown in Figure 5 in the laser gain, or optical wave amplification potential per unit distance, a quantity resulting directly from the COIL chemistry. Each position noted in this plot corresponds to an X, Y position with Z dependence integrally averaged to mimic the passage of photons through the media in the manner exhibited by the laser itself. The initial gain at time = 0 is from steady state conditions, and as is evident the development of the flow unsteadiness substantially changes the magnitude of the laser gain. At Positions 1 and 2 the gain decreases substantially, while at Position 3 it increases substantially. The explanation for this change is the change in the mixing characteristics and its subsequent impact upon the progression of the chemistry. Figure 6 shows the time, Z direction integrated average of the laser gain at various points along the X axis at the nozzle centerline in comparison with measured laser gain and that from previous steady-state simulations. In this comparison what arises is a spread of data due to the influence of advantageous and deleterious processes. Simulations using reduced chemistry mechanisms,^[6] which underestimate the influence of performance decreasing chemical reactions, tend to align with the measured gain. When the deleterious chemical reactions are included as they are in the various full chemistry mechanisms shown, the laser gain predicted falls below the measured gain.^[7] When the effects of flow unsteadiness are included using the reduced chemistry mechanism, the laser gain is over-predicted with respect to the measured laser gain. A logical interpretation of this plot is that the full complexity of the COIL physics is comprised of both the full set of chemical reactions and the flow unsteadiness.

The impact of the flow unsteadiness on the optical characteristics of the COIL media is a natural concern, given the perturbations to the media caused by the flow unsteadiness. Figure 7 shows the index of refraction, n , variation within a 2-D cut from the COIL simulation

perpendicular to the direction of optical wave propagation in the device. A value of 1 represents a vacuum, where values greater than 1 occur as optical waves pass through matter. The greater the variation and the greater the value of n , the larger the phase error incurred in the optical wave as it passes through the gas. As is shown, there are local increases near the shock waves in the supersonic region of the nozzle. However, the values of n remain very close to 1, with typical values in the 5 to 10 cm region, where the laser optical resonator resides, differing from 1 by only 1 to 2×10^{-6} , a very small difference. This is due to both the very low density of the gas, and the dominant composition of He which has a very low index of refraction relative to a vacuum.

The work of Fric and Roshko indicated that a variety of structures in the jet-in-crossflow were associated with the presence of flow unsteadiness. Among these are 'wake vortices' that project from the wall boundary layer behind the jet. Three-dimensional perspectives can help to further elucidate the wake structure prediction. The 3-D stream traces initiated upstream of the large injector orifice in the XZ plane adjacent to the wall are shown in Figure 8. In addition to the stream traces, vortex cores in this region of the 3-D space are plotted using the vortex core identification functions of Sujudi and Haines^[8] as implemented in the CFD Analyzer software from Amtec Engineering. Figure 8 shows the vortex cores in relation to the 3-D stream traces initiated in the XZ plane adjacent to the wall. While vortex cores are captured and streamlines are shown projecting downward from the wall toward the backside of the jet, no vortex cores associated with this downward projecting fluid indicate a lack of rotation. Additionally, this downward projecting fluid is adjacent to the symmetry plane at the centerline of the large injector orifice, suggesting that the symmetry plane may be interfering with the development of the 'wake' vortex structures. The absence of these structures suggests that the flow physics are not completely captured in this simulation, and that the characteristics of the flow unsteadiness may not be entirely correct.

To test this hypothesis, the COBALT₆₀ code is used to simulate the experiment of Fric and Roshko. As noted previously, no symmetry plane is used at the centerline plane of the jet orifice, allowing for full lateral development of the flow. As a side note, previous work has demonstrated that COBALT₆₀ and GASP give very similar results for unsteady test flows and this advantage is utilized here to facilitate the simulation of multiple flowfields at the same time. The 3-D COBALT₆₀ model was executed using 2nd order spatial and 2nd order temporal accuracy. The simulation was advanced in time using a time step of 1.0×10^{-7} sec and was advanced to a physical time of 0.01 sec using a total of 100,000 time steps. Figures 9 and 10 show different perspectives of an isosurface of constant vorticity magnitude with

superimposed contour variation of total pressure in the jet as determined by this simulation. Two separate vortical structures associated with flow unsteadiness as noted by Fric and Roshko in their experiments were captured in this simulation. The first are the 'wake' vortices that project from the wall behind the jet into the jet itself. These are clearly captured. The second are 'shear-layer' or 'ring' vortices that develop circumferentially about the jet but initiate at the anterior interface between the boundary layer fluid in the primary and the jet as it exits the orifice. These are also captured in the simulation. Additionally, Figure 11 illustrates the development of an odd-even pattern in vorticity behind the jet in a 2-D plane cut through the flow near the wall, where the circular structures are cross-sectional cuts through the wake vortices. This asymmetric, odd-even pattern in the vortex structure is indicative of lateral fluctuations behind the jet. The symmetry boundary plane splitting the injector orifice in the COIL simulations would interfere with the capturing of these fluctuations through the enforcement of symmetry, which, as seen here, is not consistent with the behavior in the flow about this plane. The conclusion to be drawn from this simulation is that the capture of the wake vortices noted by Fric and Roshko to a source of flow fluctuation are influenced by lateral fluctuations about the symmetry plane of the jet. This in turn confirms the observation in the COIL simulation described above that the symmetry plane boundary appears to interfere with the development of the wake vortices and thus should not be used.

The third simulation is a test of this hypothesis for the COIL nozzle configuration. Reviewing briefly, this simulation places both lateral boundaries between the small injector orifices and models these boundaries as periodic boundaries to allow for lateral fluctuations in the flow. Thus the symmetry boundary condition used previously in COIL simulation is removed. Also, the COIL diluent gas He is used to reduce the computational cost for this test that is directed toward the fluid dynamic aspects of the COIL flow.

The GASP model for this simulation was executed using 1st order temporal and 3rd order spatial accuracy. The physical timestep used was 1.0×10^{-8} sec for 55,000 timesteps, advancing the flow in time to 0.00055 sec. The flow features captured by this simulation are shown in different perspectives in Figures 12 and 13. Figure 12 shows a composite streamtraces initiated in the boundary layer upstream of the large injector orifice, vortex cores, and a Mach number = 1 isosurface in the nearfield of the orifices. The streamlines trace the primary boundary layer flow as it passes around the large injector jet and wraps around it. As the streamlines wrap around the back side of the large injector jet, they suddenly project downward with rotation in a manner consistent the wake vortex structures noted above for the Fric and Roshko

experiment simulation. Vortex cores are extracted at the center of these structures, confirming the interpretation as wake vortices. Comparing with this same plot for the reacting COIL simulation in Figure 8, vortex cores were not found in conjunction with the downward projecting streamlines, tending to confirm the analysis that the symmetry boundary condition at the centerline plane of the large injector orifice interfered with the formation of the wake vortices. Figure 13 shows the same perspective in Figure 12 from a greater distance to provide greater detail regarding the interaction between the wake vortices and the fluid from the injector orifices. As the wake vortices project downward, they impact the back side of the fluid from the injector orifice and change trajectory to follow that of the fluid from the orifices. This behavior is noted not just with the interaction of the wake vortices behind the large injector orifice with its fluid, but also with those behind the small injector orifices and the small injector jet. Examining the Mach number = 1 isosurface Figures 12 and 13 shows that the 'ring' vortices found in the simulation of the Fric and Roshko experiment as well as the experiment itself are absent from this flow. The absence of these structures may indicate a fundamental difference between the strongly compressible flow in this simulation with shock waves located in the jet structure, and the low Mach number, incompressible flowfield in the Fric and Roshko experiment, with the presence of the shocks inhibiting the formation of the 'ring' vortices.

The fluctuations associated with this interaction are shown in terms of the velocity components of the flow as taken at various monitoring points in Figures 14–16. These plots show that of the 10 monitoring points, two demonstrate large amplitude fluctuation. Both of these points are located on the backside of the jet from the large injector orifice where the interactions with the wake vortices occur. As can be seen, the fluctuations occur with all 3 velocity components. Of special note is the fluctuation in the Z direction that is perpendicular to the symmetry plane of the large injector orifice. The large amplitude of this fluctuation, entirely absent in the COIL simulation where the symmetry boundary is present, confirms the expectation that removal of the symmetry boundary condition at the centerline plane of the large injector orifice would facilitate its capture in the simulation.

The primary frequency of the fluctuations in Figures 14–16 is 36900 Hz, corresponding to a non-dimensional frequency or Strouhal number of 0.08. This value is lower than the range of 0.13 to 0.19 noted by Fric and Roshko in their experiments with incompressible flows, but the presence of the strong compressibility in this flowfield may have the effect of altering the unsteady characteristics somewhat. The absence of the 'ring' vortices in this simulation may be one manifestation of this difference. It should also be noted that this is

somewhat lower than the 147 kHz value found previously in COIL simulations.

The attention paid to this detail, while seeming trivial on the surface, is justified based upon the impact that these fluctuations have upon COIL performance. As demonstrated earlier, the fluctuations have a significant impact upon the laser gain through the mixing and chemistry. An additional impact occurs through Doppler shifts to the frequency of radiation that the atoms in the resonator field experience due to the fact that they are translating, causing a decrease in laser gain. Z direction fluctuations are significant for this particular hardware since the primary direction of transit of the radiation through the device is in the Z direction. In similar COIL hardware, fluctuations in the Y direction would be significant in this same sense because the path of optical transit is in the Y direction.

Parallel execution performance for the COBALT₆₀ and GASP codes on the IBM SP3, and GASP on the Compaq SC45 supercomputer(s) is shown in Figure 17. Parallel execution speedups are high for both codes throughout the range of measurement. The communications costs are directly attributable to the use of fully implicit integration, requiring communication of zonal boundary information after each inner iteration of the Gauss-Seidel matrix inversion solver. Communications costs increase with the number of variables tracked, explaining the higher communications costs for the 3-D GASP COIL model. Due to the domain decomposition model used by these codes for parallel execution, memory use decreases with increasing number of processors used.

In conclusion, the results provided here establish that the unit-cell approximation as previously implemented in simulations of the COIL flowfield with a symmetry plane boundary splitting an injector orifice interferes with the capture of flow structures associated with unsteadiness. Non-reacting simulations of unsteady flow experiments and of COIL hardware indicate that lateral passage of waves normal to this symmetry plane is associated with fluctuations in the flow about this plane. An additional difference is noted in a lower dominant frequency of fluctuation in the non-reacting simulation without the symmetry plane at the center of the orifice as opposed to the reacting COIL simulation; the presence of would not be expected to account for this difference. In the reacting flow COIL simulation where the symmetry plane was present, the flow unsteadiness found there was shown to have a substantial effect on the laser gain prediction.

Future work will focus on simulations utilizing the COIL chemistry model and a domain model where the lateral boundaries at both ends are periodic and are located between the small injector orifices as in the non-reacting simulation of the same described here.

4. Significance

Spatial and temporal gradients in chemical laser flowfields have direct bearing on the efficiency of the devices. Understanding the mechanisms that impact the efficient utilization of fuels in chemical lasers is critical to their application.

5. Systems Used

ASC IBM SP3 and Compaq SC45, ERDC Compaq SC45, MHPCC IBM SP3/SP4, NAVO IBM SP3/SP4.

6. CTA

Computational Fluid Dynamics (CFD)

References

1. Madden, T.J. and J.H. Miller, "Simulation of Flow Unsteadiness in Chemical Laser Flowfields." *AIAA-2004-0805*, 42nd AIAA Aerospace Sciences Meeting and Exhibit, Reno, NV, January 5–8, 2004.
2. Perram, G.P., *Int. J. Chem. Kinet.* 27, 1995, pp. 817–828.
3. Fric, T.F., and A. Roshko, "Vortical structure in the wake of a transverse jet." *J. Fluid Mech.*, 279, 1994, pp. 1–47.
4. Strang, W.Z., R.F. Tomaro, and M.J. Grismer, *AIAA Paper 99-0786*, 37th AIAA Aerospace Sciences Meeting, Reno, NV, January 11–14, 1999.
5. Miller, J.H., J.S. Shang, and T.J. Madden, *AIAA Paper 2001-2869*, 32nd AIAA Plasmadynamics and Lasers Conference, Anaheim, CA, June 11–15 June, 2001.
6. Madden, T.J. and W.C. Solomon, *AIAA 97-2387*, 28th Plasmadynamics and Lasers Conference, Atlanta, GA, June 23–25, 1997.
7. Madden, T.J., *SPIE Proceedings of XIV International Symposium On Gas Flow & Chemical Lasers and High Power Laser Conference*, Wroclaw, Poland, August 25–30, 2002.
8. Sujudi, D. and R. Haimes, "Identification of Swirling Flow in 3-D Vector Fields." *AIAA Paper 95-1715*, San Diego, CA, June 1995.

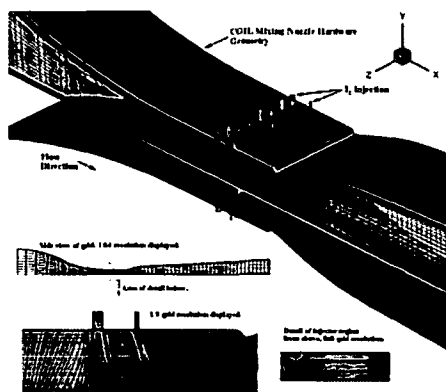


Figure 1. Computational grid used in the 3-D GASP COIL simulation, shown in relation to a rendering of the wetted surfaces in the COIL laser hardware. This grid also presents the geometric similarity used to simplify the much larger physical domain into a realistic computational domain, denoted the unit-cell.

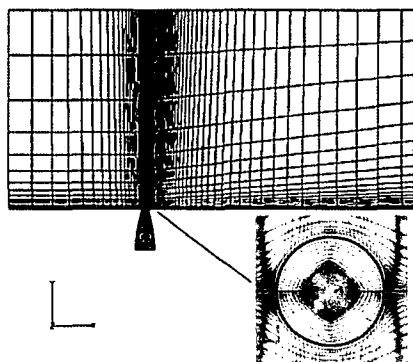


Figure 2. 2-D cuts of the 3-D computational grid used in the COBALT₆₀ simulation of the Fric and Roshko 'jet-in-crossflow' experiment

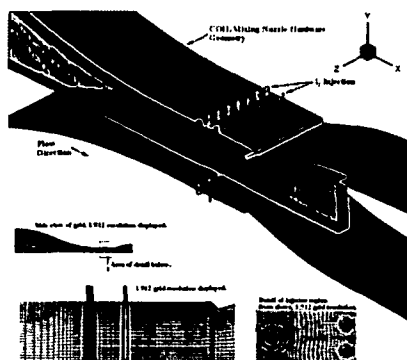


Figure 3. Computational grid used in the non-reacting 3-D GASP simulation of COIL hardware, shown in relation to a rendering of the wetted surfaces in the COIL laser hardware. Note the use of multiblock, highly orthogonal grid structure to improve grid quality over the grid used in the first simulation.



Figure 4. Fixed time snap shot of unsteady fluid dynamic structures manifested in the He/I₂ jet from the 3-D GASP COIL simulation. A surface of constant I₂ mole fraction acts as a scalar tracer for the jet structure.

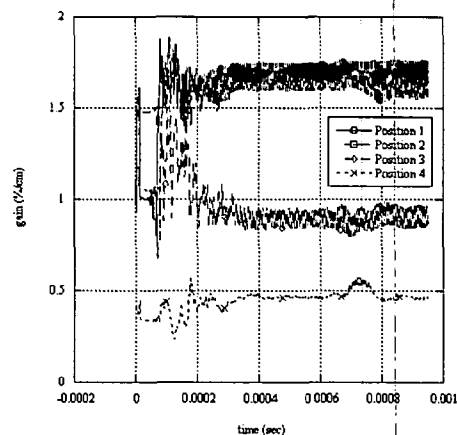


Figure 5. Time traces for the Z-averaged laser gain at different positions in the laser resonator section of the simulated COIL hardware. This data was taken at a sampling rate of 10 iterations of the 3-D GASP COIL simulation, for a temporal sampling rate of 1×10^{-7} sec.

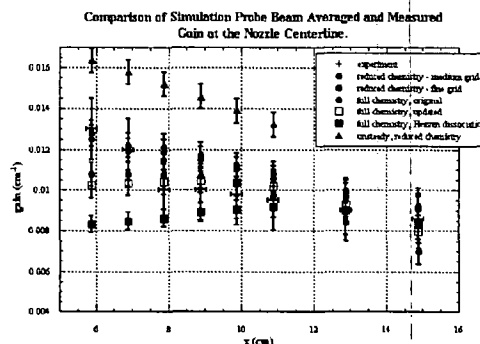


Figure 6. Comparison of time, Z-averaged laser gain from the unsteady COIL simulation with experiment data and previous steady-state COIL simulations. The steady state simulations include varying levels of chemistry modeling fidelity.

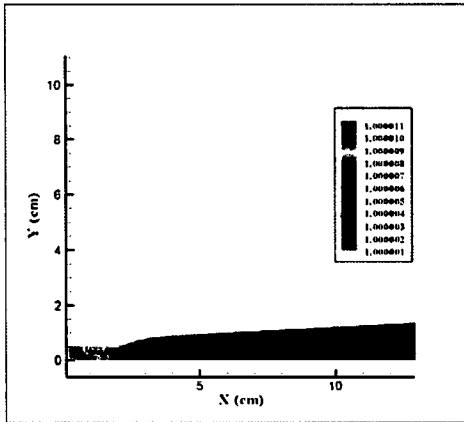


Figure 7. Index of refraction within the 2-D plane at the center of the large injector orifice from the 3-D GASP COIL simulation

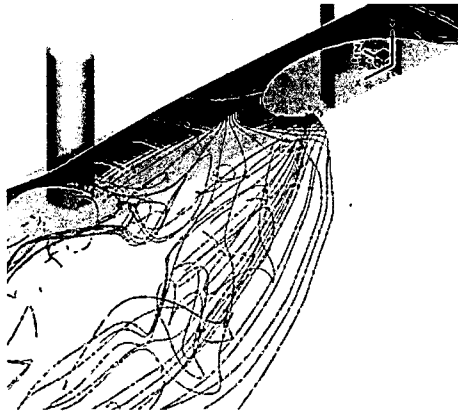


Figure 8. 3-D streamtraces (in black) initiated upstream of the large injector orifice in the first XZ plane (0.00098 cm) from the wall in conjunction with vortex cores (in red) extracted from the 3-D GASP COIL simulation.

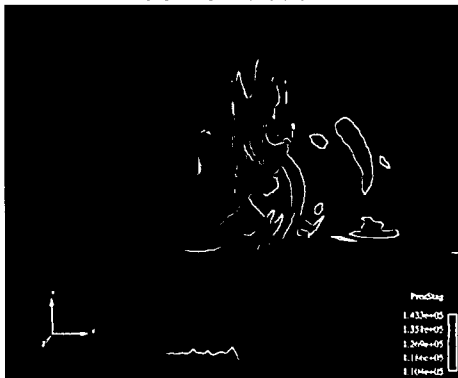


Figure 9. Isosurface of constant vorticity magnitude with stagnation pressure contours superimposed from the COBALT₆₀ simulation of the Fric and Roshko 'jet-in-crossflow' experiment. This view is from the side of the jet.

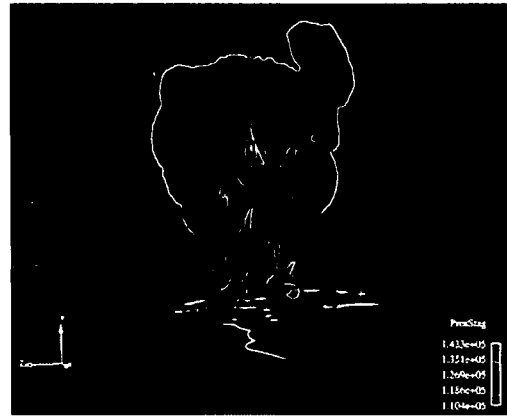


Figure 10. Isosurface of constant vorticity magnitude with stagnation pressure contours superimposed from the COBALT₆₀ simulation of the Fric and Roshko 'jet-in-crossflow' experiment. This view is from the backside of the jet.



Figure 11. Contours of vorticity with rotation normal to the wall in the near field of the jet in Figures 9 and 10. From the COBALT₆₀ simulation of the Fric and Roshko 'jet-in-crossflow' experiment.

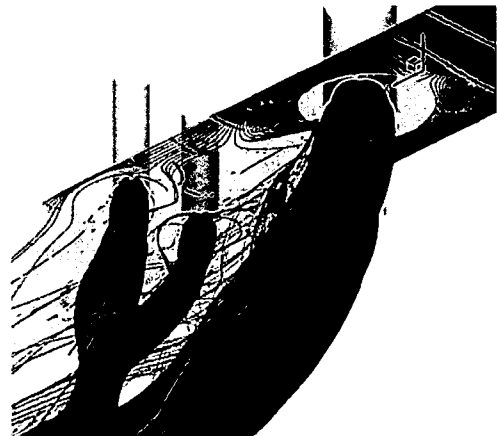


Figure 12. Streamlines, in black, vortex cores, in red, and Mach number =1 isosurface in the jet nearfield from the non-reacting COIL hardware simulation. This simulation does not use the symmetry boundary at the center of the large injector orifice as in the first simulation, but uses periodic boundaries outside of the small injector orifices.

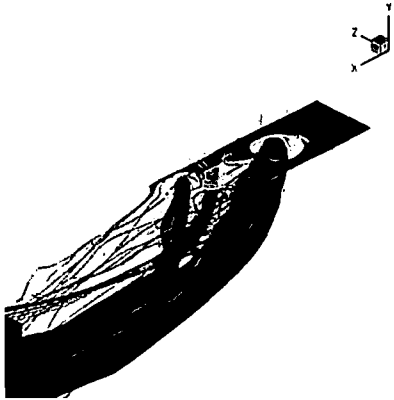


Figure 13. Streamlines, in black, vortex cores, in red, and Mach number = 1 isosurface in the jet nearfield from the non-reacting COIL hardware simulation. This simulation does not use the symmetry boundary at the center of the large injector orifice as in the first simulation, but uses periodic boundaries outside of the small injector orifices. This perspective is further removed than with Figure 12.

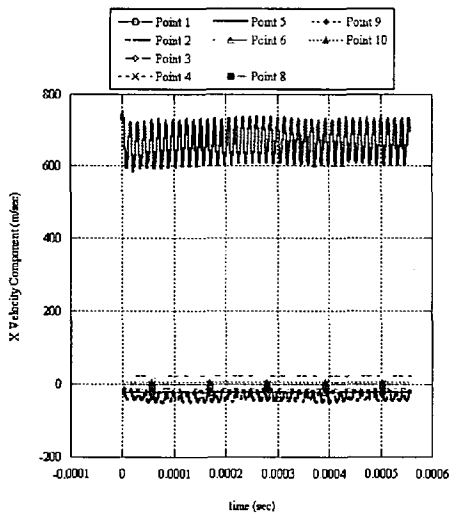


Figure 14. Time variance of the streamwise velocity (X) component at various monitoring points in the jet nearfield from the non-reacting COIL hardware simulation shown in Figures 12 and 13

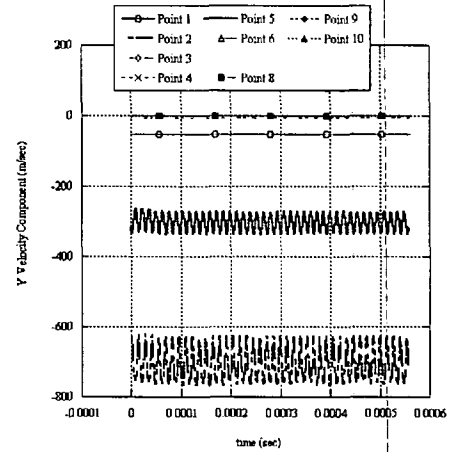


Figure 15. Time variance of the vertical velocity (Y) component at various monitoring points in the jet nearfield from the non-reacting COIL hardware simulation shown in Figures 12 and 13

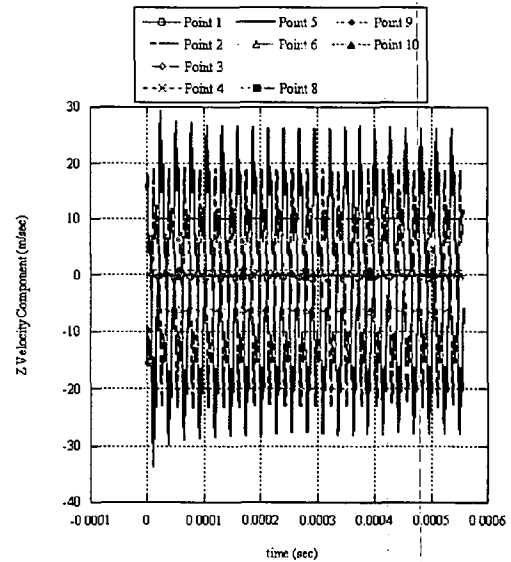


Figure 16. Time variance of the lateral velocity (Z) component at various monitoring points in the jet nearfield from the non-reacting COIL hardware simulation shown in Figures 12 and 13

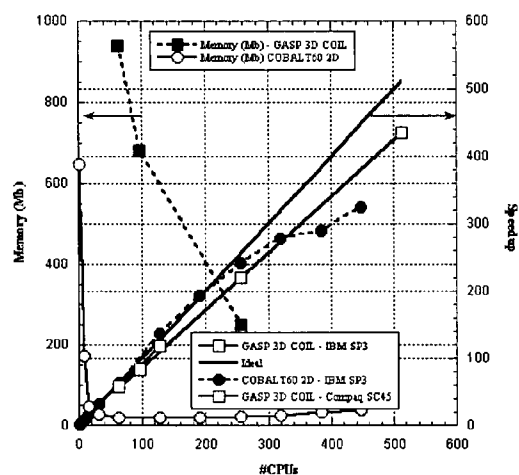


Figure 17. Speedup and memory usage for COBALT and GASP on the IBM SP3, and GASP on the Compaq SC45. Note that the COBALT timings are for a 2-D case and the GASP timings are for the 3-D COIL case.